Tectonophysics 589 (2013) 33–43

Contents lists available at SciVerse ScienceDirect

Tectonophysics

journal homepage: www.elsevier.com/locate/tecto

Determination of full moment tensors of microseismic events in a very heterogeneous mining environment

Daniela Kühn [a,*], Václav Vavryčuk [b]

[a] NORSAR, Gunnar Randers vei 15, 2007 Kjeller, Norway
[b] Institute of Geophysics, Academy of Sciences, Boční II/1401, 141 00 Praha 4, Czech Republic

ARTICLE INFO

Article history:
Received 21 March 2012
Received in revised form 2 November 2012
Accepted 23 December 2012
Available online 12 January 2013

Keywords:
Moment tensors
Non-double-couple components
Microseismicity
Mining
Finite-difference modelling
Scattering

ABSTRACT

The determination of source parameters and full moment tensors in mines is a difficult task, especially, when the velocity model of the mining environment is complex and strongly heterogeneous. The heterogeneities in the velocity model are usually caused by the presence of ore bodies, host rocks, tunnel systems and large excavations due to mining activity. The mined-out cavities introduce strong velocity contrasts in the model, cause multiple scattering of waves and result in a complex wave field with long coda waves. We have analysed five blasts and five induced microseismic events recorded at the Pyhäsalmi ore mine, Finland, and suggest a strategy of successfully inverting for the seismic moment tensors. We compute accurate locations using an eikonal solver and perform the time-domain moment tensor inversion from full waveforms using a generalized linear inversion. Green's functions are computed using a 3-D finite difference visco-elastic code capable of reproducing complex interactions of waves and structures. To suppress the sensitivity of the inversion to inaccuracies of locations and the velocity model, we analyse the data in the frequency range from 30 to 80 Hz. The analysis of blasts and microseismic events proves that the moment tensor inversion is successful. The moment tensors of blasts display a high percentage of positive isotropic components. However, the presence of minor shear faulting triggered during blasting cannot be excluded. On the other hand, the moment tensors of microseismic events display significant negative isotropic and compensated linear vector dipole components. This indicates that the predominant mechanism of the events is probably related to the collapse of rock due to mining activity.

1. Introduction

Human activities in the subsurface generate changes in stress, pore pressure, volume and load, which may induce microseismicity. Long-term microseismic monitoring has the potential to reveal fracture geometry (e.g., Phillips et al., 1998, 2002; Rutledge et al., 1998; Urbancic and Rutledge, 2000), to provide useful input for safety and hazard assessments in case of mining areas and nuclear waste disposal sites (e.g., Domański et al., 2002; Luo et al., 2001; Spottiswoode and Milev, 1998) and to optimise production in case of hydrocarbon reservoirs and geothermal sites. Microseismic monitoring is frequently used to extract information on event locations and in recent years also to determine other source parameters such as focal mechanisms and seismic moment tensors (e.g., Dahm et al., 1998, 1999; Jost et al., 1998; Trifu et al., 2000; Vavryčuk, 2007; Vavryčuk et al., 2008).

The analysis of seismic moment tensors is particularly important for mining data. Contrary to natural earthquakes, where the geological environment and character of loading favour shear slip along a fault, the occurrence of non-shear processes is expected for seismic events induced in mines. High stress concentrations and the existence of mined-out cavities cause excavated volumes to collapse and enable implosive events. This specific source process is reflected by the presence of significant non-double-couple components of moment tensors (Rudajev and Sileny, 1985; Wong and McGarr, 1990; Wong et al., 1989). Hence, the evaluation of the double-couple (DC) and non-double-couple (non-DC) components of moment tensors can serve as detection tool for rock-mass fracturing (Šílený, 2009a) and can help the physical understanding of the fracture process (Julian et al., 1998; Miller et al., 1998). Microseismic data available from mines often are of good quality due to the installation of many multi-component instruments and short propagation paths through rocks virtually free of weathering effects (Miller et al., 1998).

The accurate determination of moment tensors and their non-DC components is an involved and data-demanding procedure. The moment tensor inversion requires a good knowledge of source location and velocity model, and the observations must exhibit good focal sphere coverage. Otherwise, the inversion becomes unstable and the non-DC components might be erroneous or unreliable (Šílený, 2009b; Šílený and Milev, 2008; Vavryčuk, 2007). Obviously, the results are also sensitive to the inversion scheme applied (Vavryčuk

* Corresponding author. Tel.: +47 63805 933; fax: +47 63818 719.
E-mail addresses: daniela@norsar.no (D. Kühn), vv@ig.cas.cz (V. Vavryčuk).

0040-1951/$ – see front matter © 2013 Elsevier B.V. All rights reserved.
http://dx.doi.org/10.1016/j.tecto.2012.12.035

and Kühn, 2012) as well as to frequency band and type of waves inverted.

In this paper, we focus on the moment tensor inversion of seismic events in mines characterised by a complex and heterogeneous structure. The heterogeneities in velocity models of mines are usually caused by the presence of ore bodies, host rocks, tunnel systems and large excavations due to mining activity. In particular, the mined-out cavities introduce strong velocity contrasts in the model. They represent obstacles to seismic waves, causing multiple scattering, and result in a complex wave field with long coda waves. We have analysed five mining blasts and five induced microseismic events recorded in 2003 at the Pyhäsalmi ore mine, Finland (Oye et al., 2005) and demonstrate the implications on the moment tensor inversion when complexities in the velocity model are neglected. We use numerical modelling to illustrate how P-wave polarities and amplitudes can easily be misinterpreted and how waveforms are distorted by the presence of heterogeneities. Finally, we suggest a strategy to determine accurate event locations in complex mining environments and to invert for moment tensors with reliable DC as well as non-DC components.

2. Pyhäsalmi ore mine

The Pyhäsalmi ore mine in central Finland (exploited by the Inmet Mining Co.) extends to a depth of 1.4 km and is the deepest of its kind in Western Europe. Massive sulphide ores are located in the hinge of a large synform surrounded by felsic volcanics (Puustjärvi, 1999). The ore forms a potato-shaped body; its outer rim pyrite contains zinc, the inner rim pyrite contains copper and the innermost part of the ore body consists of pyrite.

There are no distinct faults within the current mining area (depth 1100–1450 m), but active faults exist outside the mining area and near the Earth's surface. Also pegmatite veins situated near the ore contacts have been identified as possible fault planes. Stress measurements were performed before mining was commenced below the depth of 1000 m. The main stress is horizontal compression (Ledger, 1999) at N310°E with a vertical stress of 33 MPa and with maximum and minimum horizontal stresses of 65 MPa and 41 MPa, respectively. The stress agrees with the tectonic stress directions in Western Europe (Reinecker et al., 2004). The mine is quarried by sublevel and bench stoping, achieving an annual production of about 1.3 Mt of ore.

The microseismic monitoring network was installed by the ISS International Ltd. The microseismic activity is strongest throughout the tunnel system and in stopes after excavation. The most seismically active regions correspond to a chute as well as the most active mining area. Approximately 1500 events per months are detected, 2/3 of them being production blasts. Sixteen 4.5 Hz geophones, thereof four 3-C sensors, are cemented in boreholes drilled vertically in the roofs of the tunnels and have been recording since January 2003. The network was upgraded with two additional 3-C sensors in 2004. The maximum sampling rate is 3000 Hz, but records may be down-sampled depending on the main frequency of the events. Moment magnitudes range from −1.8 to 1.2, with most events varying from −1.5 to −0.5. Typical source-receiver distances are 60–400 m. At short distances, P- and S-wave signals are short and impulsive, at distances exceeding 200 m, large parts of the energy are transferred into the P- and S-wave coda, most probably due to the high level of scattering produced by interfaces with strong velocity contrasts (for more details, see Oye et al., 2005).

The mining infrastructure including tunnels, mining cavities and passes was repeatedly laser scanned, and a detailed 3-D velocity model was built using mine design software. We generated a simplified velocity model excluding tunnels using 3-D ray tracing modelling software (Vinje et al., 1996a,b). Fig. 1 shows a sketch of the mine infrastructure; Fig. 2 shows the mine model of the ore body (light brown) and cavities (darker brown) in a side and a map view together with sensor locations. The observed microseismic data under study were recorded in 2003, and they consist of five blasts and five induced

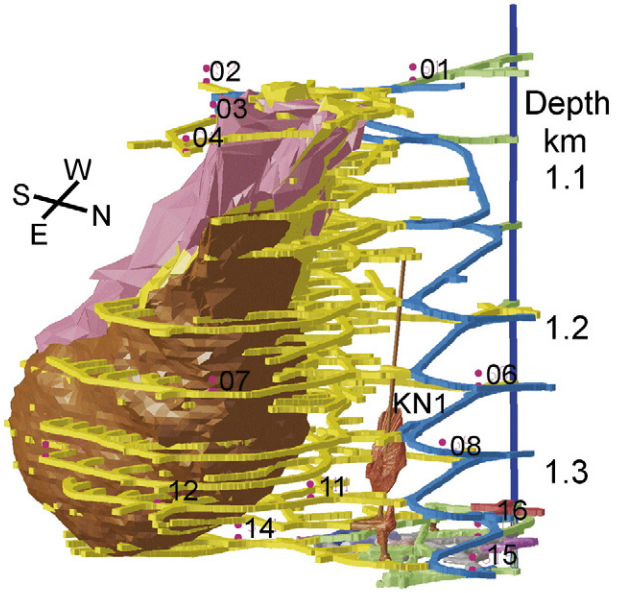

Fig 1. Model of the Pyhäsalmi ore mine; pink: zinc ore body, brown: copper ore body, yellow: access tunnels; turquoise: main road, dark blue: elevator shaft; red line (KN1): ore pass expanded in the direction of minimum horizontal stress; geophones marked by pink dots and numbers.

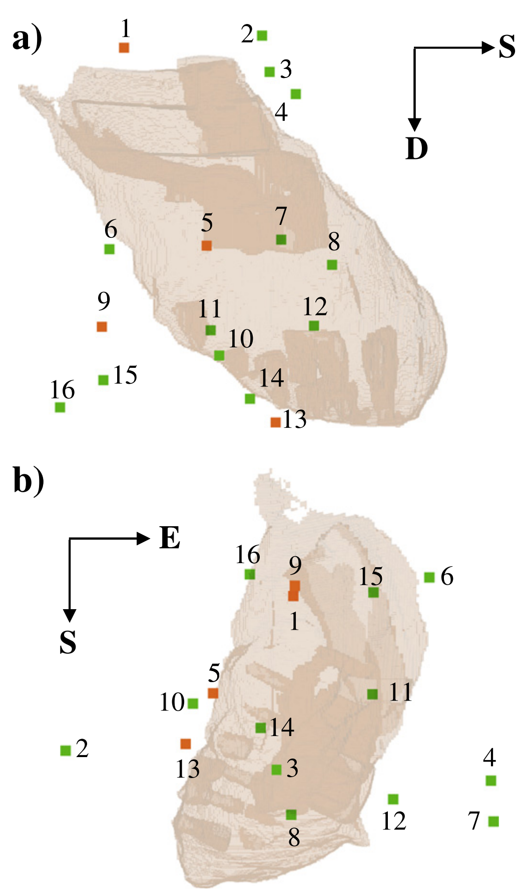

Fig. 2. Seismic network of geophones. a) View to the east; b) view from the top. Orange/green dots show the 3-component/1-component sensors, respectively.

Table 1
Blasts and events selected for moment tensor inversion.

	Date	Origin time	Magnitude	Location		
	(yyyy-mm-dd)	(hh:mm:ss)	M_W	East [m]	North [m]	Depth [m]
Blasts						
Blast 1	2003-01-14	21:59:24.4	0.9	8318	2290	−1243
Blast 2	2003-06-04	21:55:04.1	1.2	8377	2198	−1255
Blast 3	2003-06-06	21:59:25.3	1.1	8218	2129	−1346
Blast 4	2003-06-16	21:52:58.3	1.0	8160	2144	−1356
Blast 5	2003-06-19	22:03:04.4	1.0	8196	2138	−1372
Events						
Event 1	2003-05-03	06:13:43.1	0.1	8306	2320	−1241
Event 2	2003-06-13	18:07:07.7	0.0	8327	2391	−1345
Event 3	2003-06-15	05:47:22.6.	−0.1	8319	2392	−1339
Event 4	2003-08-02	05:48:52.1	0.0	8318	2349	−1055
Event 5	2003-08-27	20:15:59.9	0.0	8309	2393	−1338

events (see Table 1). Fig. 3 shows an example of waveforms filtered from 5 to 400 Hz, recorded for a mining blast (left) and a microseismic event (right). In both instances, the complexity of the wave field is distinct. Although the blast is supposed to possess a simple source mechanism of explosive character, the vicinity of its location to a cavity wall may result in ringing and complex coda waves. For the event, the increasing complexity of the waveforms with increasing distance from the event location indicates the influence of the travel paths on the waveforms.

3. Preliminary data analysis

First, we performed a simple preliminary analysis simulating a standard routine procedure. The data are filtered from 5 to 400 Hz. The preliminary locations (Table 1) were found by manually measuring P- and S-wave arrival times and using a linearised inversion (Oye and Roth, 2003) employing a homogeneous velocity model with P- and S-wave velocities of $\alpha = 5500$ m/s and $\beta = 3500$ m/s, respectively. The use of the homogeneous model was justified by observations of Gharti et al. (2010), who demonstrated that event locations calculated using homogenous and 3-D velocity models are in fairly good agreement. This implies that the impact of scattering due to inhomogeneities is more pronounced on amplitudes and the complexity of seismic traces and less pronounced on travel times. Subsequently, first onset polarities and amplitudes of P-waves were picked and inverted for full moment tensors according to Manthei (2005). The algorithm is based on the Aki and Richards (2002) formulas and provides full moment tensors using standard linear inversion. The velocity model is the same as in the location procedure.

Adopting this procedure, however, results in difficulties during the inversion. For some events, the distribution of polarities on the focal sphere is so inconsistent that no solution predicting observed polarities can be found. Fig. 4 shows the 3-D model of the Pyhäsalmi ore mine, the locations of the five analysed blasts, the positions of sensors and the corresponding focal sphere coverage. Fig. 5 presents a similar illustration for the five induced events analysed. The inconsistent distributions of polarities may have several origins. For example, the picked amplitudes may not belong to the direct wave. If the model is inhomogeneous with strong contrast interfaces, the wave field is complex and the polarities and amplitudes of the direct waves can easily be misinterpreted. Also, the inconsistent distribution of polarities may not arise from an erroneous polarity, but from erroneously determined positions of polarities on the focal sphere due to the assumption of a homogeneous velocity model. While the ray paths are straight lines in the homogeneous velocity model, the real ray paths may be curved. Obviously, a complicated 3-D velocity model characterised by the presence of large excavation areas with a complicated geometry and strong velocity contrasts (see Table 2) can distort not only the P-wave polarity pattern on the focal spheres, but also the P-wave amplitudes as well as the complete wave field.

To understand the origin of the inconsistent polarity distributions, we employ 3-D finite-difference modelling of waveforms for the Pyhäsalmi ore mine velocity model. Using real as well as synthetic sensor configurations, we test the sensitivity of the P-wave polarities, amplitudes and waveforms to source locations and velocity model numerically, and we study the influence of these effects on P-wave polarity patterns on the focal sphere.

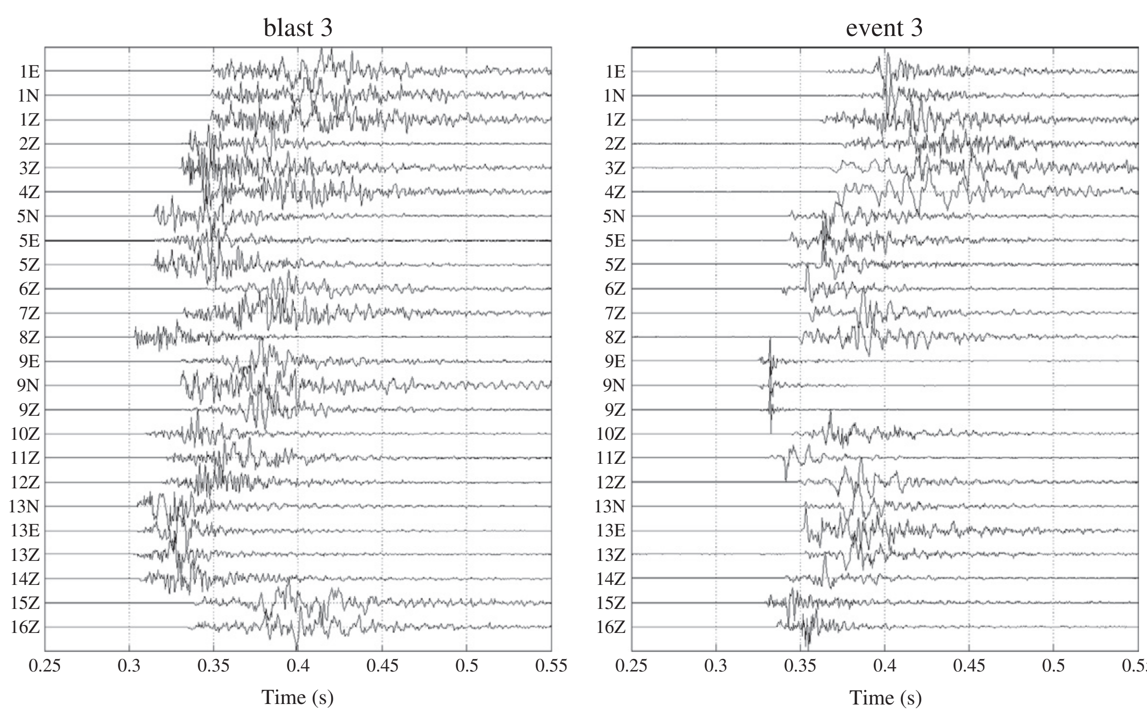

Fig. 3. Examples of waveforms for a mining blast (left; blast 3) and a microseismic event (right; event 3). Sensor numbers and component indicated in front of each trace.

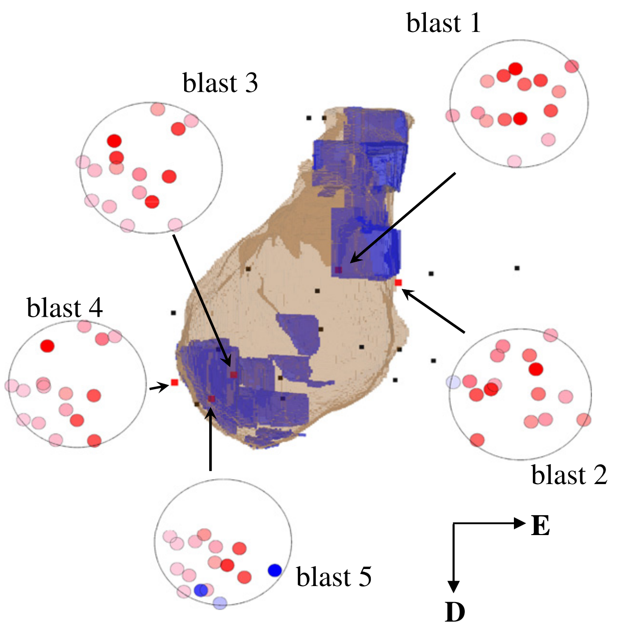

Fig. 4. Distribution of P-wave polarities on the focal sphere for five selected blasts. Middle: Pyhäsalmi mine model (view to the north), brown: ore body, blue: mined-out cavities, host rock not displayed; geophones are marked by black dots. Figures at the margin: polarity distribution for blasts marked by red dots in the mine model (see arrows) in a lower hemisphere projection; circles filled in red: positive P-wave polarity, circles filled in blue: negative P-wave polarity; colour saturation corresponds to amplitude.

4. Modelling of waveforms

The 3-D finite-difference modelling of waveforms is performed using the visco-elastic code E3D (Larsen and Grieger, 1998) as implemented by Gharti et al. (2008). The implemented code includes additional routines for considering various source-time functions, visualisations with the open-source visualisation package ParaView,

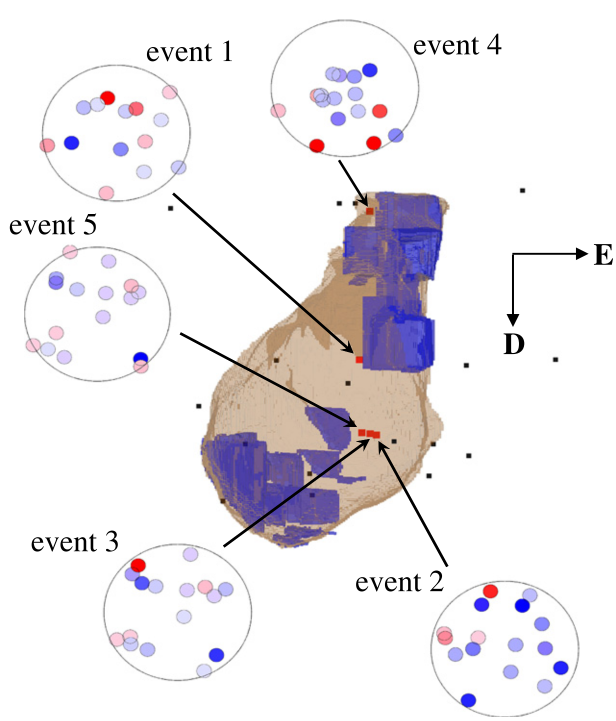

Fig. 5. Same as Fig. 4, but for the selected events.

Table 2
Parameters of the velocity model.

	v_P [m/s]	v_S [m/s]	ρ [kg/m^3]
Excavation area	300	0	1
Host rock	6000	3460	2000
Ore body	6300	3700	4400

and routines for computing the strain Green's tensor. In the following, we demonstrate on several examples how the complex 3-D velocity model may affect the wave field and thus the moment tensor inversion. Gharti et al. (2008) evidence the strong interaction of the wave field with the mined-out cavities resulting in reflections, conversions and multiple scattering. The first arrivals behind the mined-out cavities consist of wavefronts diffracted around the cavity and amplitudes of P-wave first arrivals are reduced significantly in the shadow zones behind the cavities. Since the heterogeneities are of the same order or smaller than the wavelengths of typical microseismic signals, the wavefronts heal quickly after passing the cavity, which means that travel times are affected only marginally.

In the following, we analyse the amplitude variations caused by shadow zones behind cavities and their effects on moment tensor inversion. The velocity contrasts are defined in Table 2. Fig. 6 shows a comparison between the seismic traces recorded by a fictitious seismic network computed using the homogeneous velocity model and the 3-D inhomogeneous velocity model. The network was designed in order to record a dense and uniform distribution of amplitudes excluding the influence of source-receiver distance. The 3-component records are shown for two sensors. Positive and negative P-wave first onsets are marked by a vertical red and blue line, respectively. The seismic traces for the homogeneous model are very simple and both polarities and amplitudes change as expected (amplitudes being weaker near the nodal planes). The synthetic records generated using the 3-D velocity model are much more complex, featuring both long P- and S-coda waves. The distribution of amplitudes on the focal sphere is more irregular. The P-wave first onset amplitude is significantly reduced at sensor 1 compared to the homogeneous model. At sensor 2, the P-wave polarity has even been reversed.

Fig. 7 shows the results of a numerical experiment on the influence of material properties within the cavities. First, the cavity is filled up with a material having the same properties as the surrounding ore body, hence the only velocity contrast in the model is between the ore body and host rock (Fig. 7a). Subsequently, the seismic velocities are reduced stepwise (only a selection of results is presented). For each case, the trace of the same vertical sensor is displayed and the amplitudes for all sensors are shown on the focal sphere. When seismic velocities decrease within the cavities, the amplitude of the P-wave decreases and finally changes its polarity. In general, the waveforms as well as the distribution of amplitudes and polarities over the focal sphere vary significantly.

Fig. 8 displays the influence of source location on the P-wave polarity distribution on the focal sphere. The middle panel pictures the mine model and two different source positions with slightly differing proximity to the cavity above. The positions of sensors reflect the configuration of the real seismic network. The two focal sphere plots illustrate the P-wave first motion amplitudes for the two alternative source positions. Although the vertical separation of both sources is very small, polarities have reversed at four sensors, namely the ones situated above the nearby cavity. To explain the reversed polarities, we plot P-wave first onset 'fat' rays for both sources (Červený and Soares, 1992; Hagedoorn, 1954; Husen and Kissling, 2001). A fat ray occupies the first Fresnel volume where a constructive interference of seismic energy occurs. This means that scattering from each point within this volume contributes to the recorded signal. Fig. 9 shows the fat rays for both sources in a map view from below and a depth section. For the deeper source, the P-wave first arrival consists of

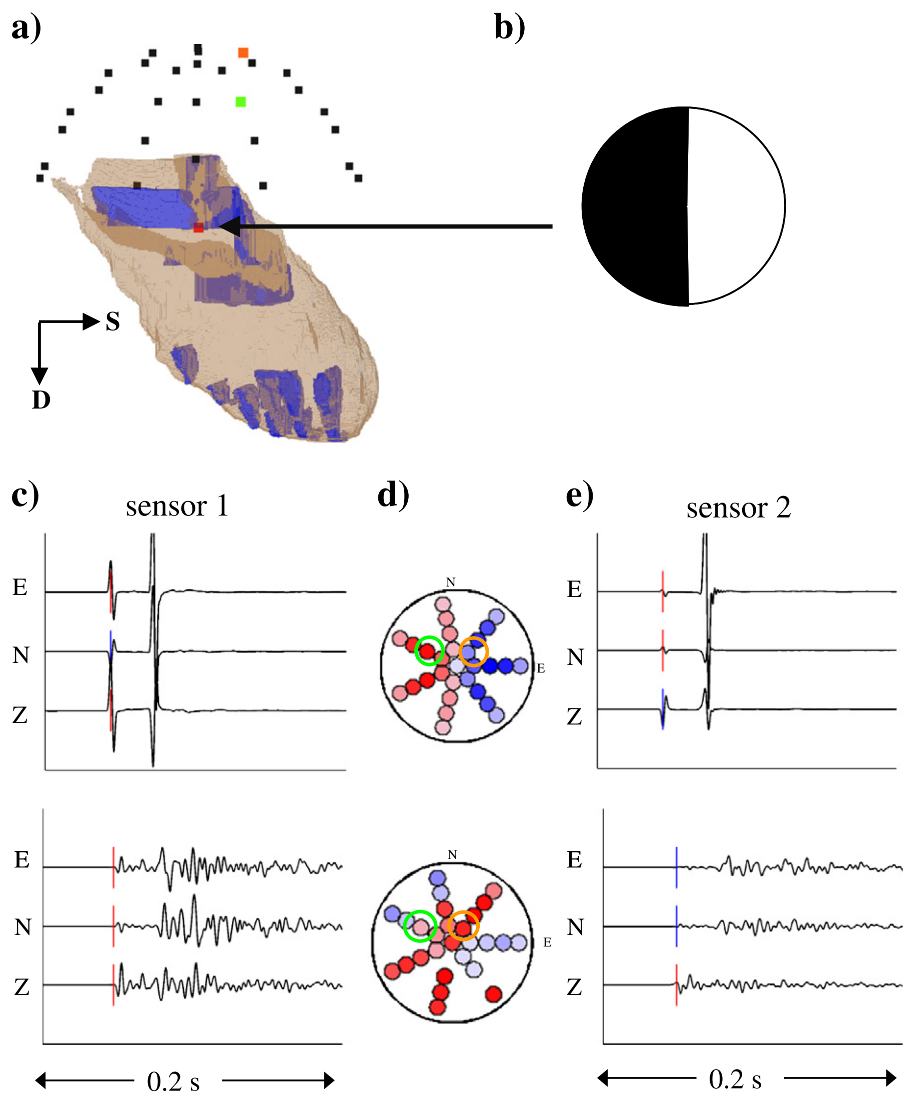

Fig. 6. Seismic traces computed in the homogeneous and the 3-D velocity model: a) Pyhäsalmi mine model, red dot: source location, black dots: artificial seismometer network constituting a half sphere on top of the mine, green and orange dots: sensors 1 and 2, respectively; b) focal mechanism assumed in the modelling; c) top: E, N and Z traces computed in the homogeneous velocity model for sensor 1, bottom: E, N, Z traces for sensor 1 computed using the 3-D velocity model; d) top: P-wave polarity distribution on the focal sphere (lower hemisphere projection) in the homogeneous velocity model, polarities measured at sensors 1 and 2 are marked by a green and orange circle, respectively, bottom: P-wave polarity distribution in the 3-D velocity model (gap in the distribution means that P-wave polarity could not be picked); e) top: E, N, Z traces for sensor 2 computed in the homogeneous velocity model, bottom: E, N, Z traces for sensor 2 computed in the 3-D velocity model.

the energy diffracted from the opposite site of the cavity as compared to the source located closer to the cavity floor. This means that the energy stems from opposite sides of the focal sphere and thus results once in a positive and once in a negative first arrival.

Based on the above numerical experiments, we conclude that the velocity model characterised by the presence of large excavation areas of complicated geometry renders the moment tensor inversion particularly difficult. The direct P-waves can be lost or become invisible in the waveforms, and the first onset can easily be misinterpreted. The P-wave polarities can be reversed due to diffraction near the source. The positions of P-wave first onset polarities on the focal sphere can be remarkably different from that for a homogeneous velocity model due to ray bending. The waveforms are extremely sensitive to the source positions. Similar distortions of the P-wave radiation pattern by structure are reported by McNally and McEvilly (1977) and Wallace et al. (1982). McNally and McEvilly (1977) observed systematically inconsistent P-wave first motions near nodal planes at the San Andreas fault due to lateral refraction of P-waves along the fault zone. Wallace et al. (1982) noticed a reversal of P-wave polarities between short- and long-period waveforms at the same station, which can be explained by a distortion of the radiation pattern both in azimuth and take-off angle due to a low velocity body within the Long Valley caldera.

Hence, the only way of performing the moment tensor inversion successfully is to take into account the true 3-D velocity model in all steps of the inversion: when computing accurate locations and accurate Green's functions. Moreover, we have to choose an inversion scheme which is robust and not very sensitive to inaccuracies in the model. Thus, we will replace the inversion of high-frequency P-wave amplitudes by the inversion of full low-frequency waveforms.

5. Relocation procedure

Since the moment tensor inversion may be sensitive to event locations as shown in the previous section, we first perform an accurate relocation of the selected blasts and events. The relocation is

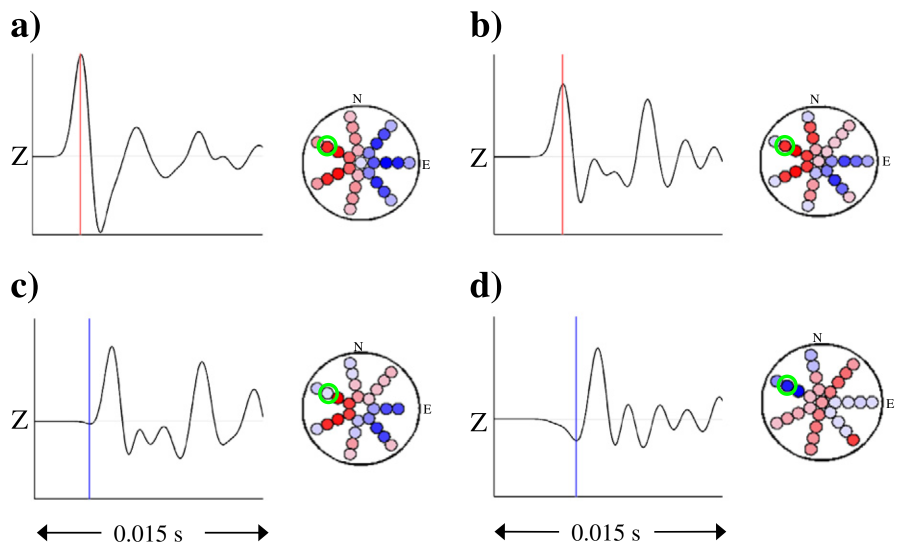

Fig. 7. Waveforms and polarity patterns for models with varying material properties within the cavity. Left: vertical trace, red and blue vertical lines mark the picked positive and negative P-wave first motions, respectively. Right: P-wave polarity distribution. Green circle marks the sensor for which the trace is displayed. Material properties within cavities are: a) $\alpha = 6300$ m/s, $\beta = 3700$ m/s (same as the ore body), b) $\alpha = 4500$ m/s, $\beta = 2600$ m/s, c) $\alpha = 4000$ m/s, $\beta = 2310$ m/s, d) $\alpha = 2000$ m/s, $\beta = 1150$ m/s.

performed by applying a full grid search using travel time tables computed with an eikonal solver. The blasts and events were selected to have a good signal-to-noise ratio, so that the arrival times are measured with high accuracy.

The eikonal solver (Podvin and Lecomte, 1991) takes into account refractions and diffractions of the wave field and provides accurate first P- and S-wave arrival times even in very heterogeneous media. The principle of reciprocity was employed in computing the travel time tables: receiver positions were considered as source locations and travel times were stored at all grid points. The objective function minimized during the location process was defined as the sum over the squared differences between the S–P times observed and computed at the receivers. The S–P times were adopted in order to exclude the influence of the unknown origin time of the event. Figs. 10 and 11 display the locations of the selected blasts and events within the mine model. Due to their origin, the blasts are situated much closer to the cavities than the events. Table 3 summarizes the shifts in event locations between homogeneous and 3-D velocity model. In most cases, the shift in the horizontal direction is much larger than in the vertical direction, contrary to the larger uncertainty in depth location detected by Gharti et al. (2010). As opposed to Gharti et al. (2010) who found good agreement in locations using the homogeneous velocity model and the 3-D velocity model employing a migration-based location algorithm, the shifts in event locations between homogeneous and 3-D velocity model using a full grid search are substantial. Unfortunately, we do not have access to the true locations of the blasts for comparison. The accurate locations of the blasts and the events are employed for the moment tensor inversion described in the following section.

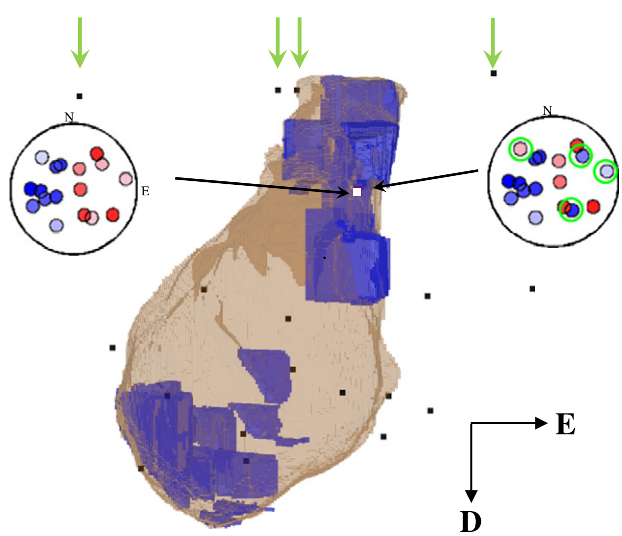

Fig. 8. P-wave polarity distributions for two events with nearby locations. Middle: model of the mine; left: P-wave polarities on focal sphere for deeper source, right: P-wave polarities for source closer to cavity floor. The sources are marked by white dots in the mine model. Green circles mark the sensors at which the polarity has changed. These sensors are indicated by green arrows in the mine model.

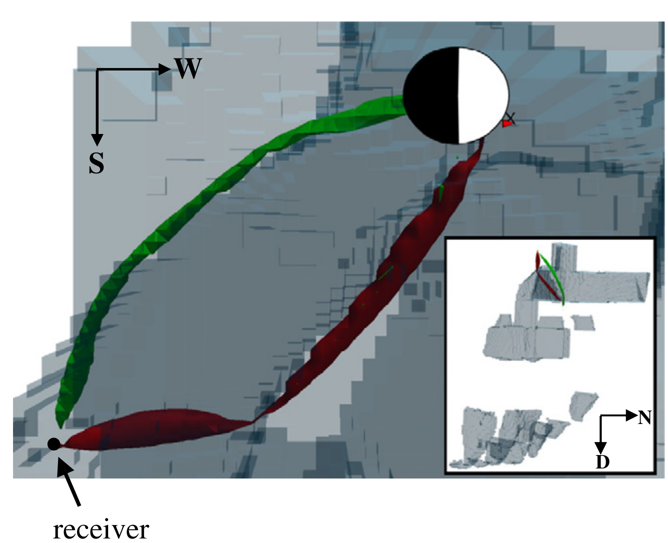

Fig. 9. Fat rays for deeper source (green) and source located closer to cavity floor (red). Large picture: map view from below, inset: depth section showing the mined-out cavities. The moment tensor assumed in modelling the synthetic data is displayed as beach-ball in a lower hemisphere projection.

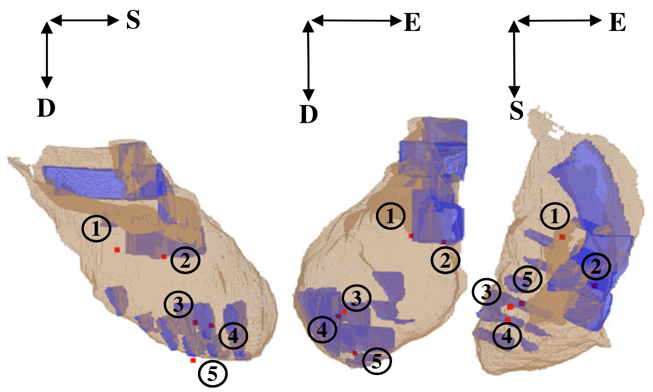

Fig. 10. Relocation of blasts. Left: view to the east, middle: view to the north, right: top view; red dots: locations of the blasts (see Table 3 for details). Figure scales are not comparable; arrow lengths correspond to 100 m.

Table 3
Relocation of blasts and events using the 3-D velocity model.

	Shift east [m]	Shift north [m]	Shift depth [m]	Total shift [m]	East [m]	North [m]	Depth [m]
Blasts							
Blast 1	−12	22	5	26	8306	2312	−1238
Blast 2	−23	36	5	43	8354	2234	−1250
Blast 3	24	63	−6	68	8218	2192	−1352
Blast 4	54	24	0	59	8214	2168	−1356
Blast 5	36	56	−42	79	8232	2194	−1414
Events							
Event 1	12	−6	9	16	8318	2314	−1232
Event 2	5	−139	57	150	8332	2252	−1288
Event 3	15	−36	27	47	8334	2356	−1312
Event 4	10	−23	3	25	8328	2326	−1052
Event 5	25	−31	0	40	8334	2362	−1338

6. Moment tensor inversion of waveforms

We invert five blasts and five microseismic events (see Table 1) for full moment tensors. All blasts and events are recorded on 21 to 24 channels with a good signal-to-noise ratio and good focal sphere coverage. The records were re-sampled to a uniform sampling rate matching the Green's functions. Green's functions are computed using the 3-D finite difference visco-elastic code E3D (Larsen and Grieger, 1998) as implemented by Gharti et al. (2008). The spatial sampling is 2 m, thus the sampling frequency is 10 kHz. The central frequency of the Gaussian source pulse is 350 Hz. Both Green's functions and data are filtered by a high-pass two-sided Butterworth filter with a corner frequency of 30 Hz to remove low-frequency noise.

We use a waveform inversion performed in time domain, where the actual time-dependence of the source-time function is neglected, assuming it to be the Dirac delta function (Sokos and Zahradník, 2008; Vavryčuk and Kühn, 2012). In this case, the time convolution in the representation theorem (Aki and Richards, 2002, Eq. (3.23)) is reduced to multiplication, and the moment tensor is calculated in the time domain using a system of linear equations employing a generalized linear inversion (Menke, 1989). The inversion is performed for the time-independent moment tensor **M**, and the equations include amplitudes recorded at all stations and at all times. The inversion is performed in two steps. After the first iteration, the observed and synthetic waveforms at each sensor are cross-correlated in order to find their optimum alignment. The waveforms are shifted in time to yield the highest correlation with synthetics. The time shifts must lie within the range of −0.01 s to 0.01 s. This procedure suppresses errors in arrival times produced by a slightly inaccurate location or an inaccurate velocity model. During the second iteration, the inversion procedure is applied to the optimally aligned waveforms. The waveforms at the three sensors featuring the worst fit between data and synthetics are automatically omitted. Such a procedure appears to be robust and insensitive to noise and inaccuracies in the velocity model (Vavryčuk and Kühn, 2012). The inversion works properly if the waveforms are filtered to remove high frequencies and thus suppress effects connected to the source-time history. Therefore, both waveforms and Green's functions are filtered to have an identical frequency content using a two-sided low-pass Butterworth filter with a corner frequency of 80 Hz.

The errors of the inversion are estimated using repeated inversions of waveforms contaminated by random noise with a uniform statistical distribution. The level of noise is 30% of the maximum amplitude of the noise-free waveform, and the inversion is performed 100 times. The resultant moment tensors are decomposed into double-couple and non-double-couple components and the P and T axes of the double-couple part are calculated. The errors in orientation of focal mechanisms are estimated from the scatter of P/T axes. They are computed as the mean of the deviations between P/T axes calculated for the noise-free solution and P/T axes measured for the 100 noisy solutions using:

$$\delta(\mathrm{P/T}) = \frac{1}{2}(\delta\mathrm{P} + \delta\mathrm{T}),$$

$$\delta\mathrm{P} = \frac{1}{100}\sum_{n=1}^{100}\frac{180}{\pi}\,\mathrm{acos}\left(\mathbf{p}^0\cdot\mathbf{p}^n\right),\ \ \delta\mathrm{T} = \frac{1}{100}\sum_{n=1}^{100}\frac{180}{\pi}\,\mathrm{acos}\left(\mathbf{t}^0\cdot\mathbf{t}^n\right),$$

where $\mathbf{p}^0$, $\mathbf{t}^0$ and $\mathbf{p}^n$, $\mathbf{t}^n$ are unit direction vectors of P and T axes for the noise-free solution and the nth noisy solution, respectively. The errors in the double-couple (DC), isotropic (ISO) and compensated linear vector dipole (CLVD) percentages are calculated as standard deviations of the 100 noisy solutions. Since the noise level of 30% used in the calculations is chosen arbitrarily, the errors have no physical background and should be viewed as rough estimate of the stability of the inversion.

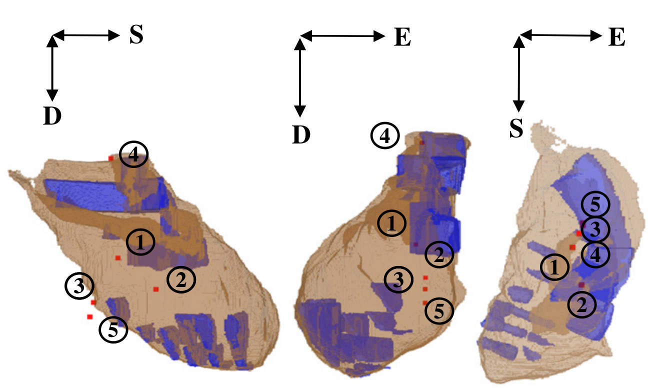

Fig. 11. Same as Fig. 10, but for the relocation of events.

7. Results

The results of the moment tensor inversion are shown in Figs. 12 and 13 and summarized in Table 4. The figures show P-wave radiation patterns, orientations of the double-couple components as well

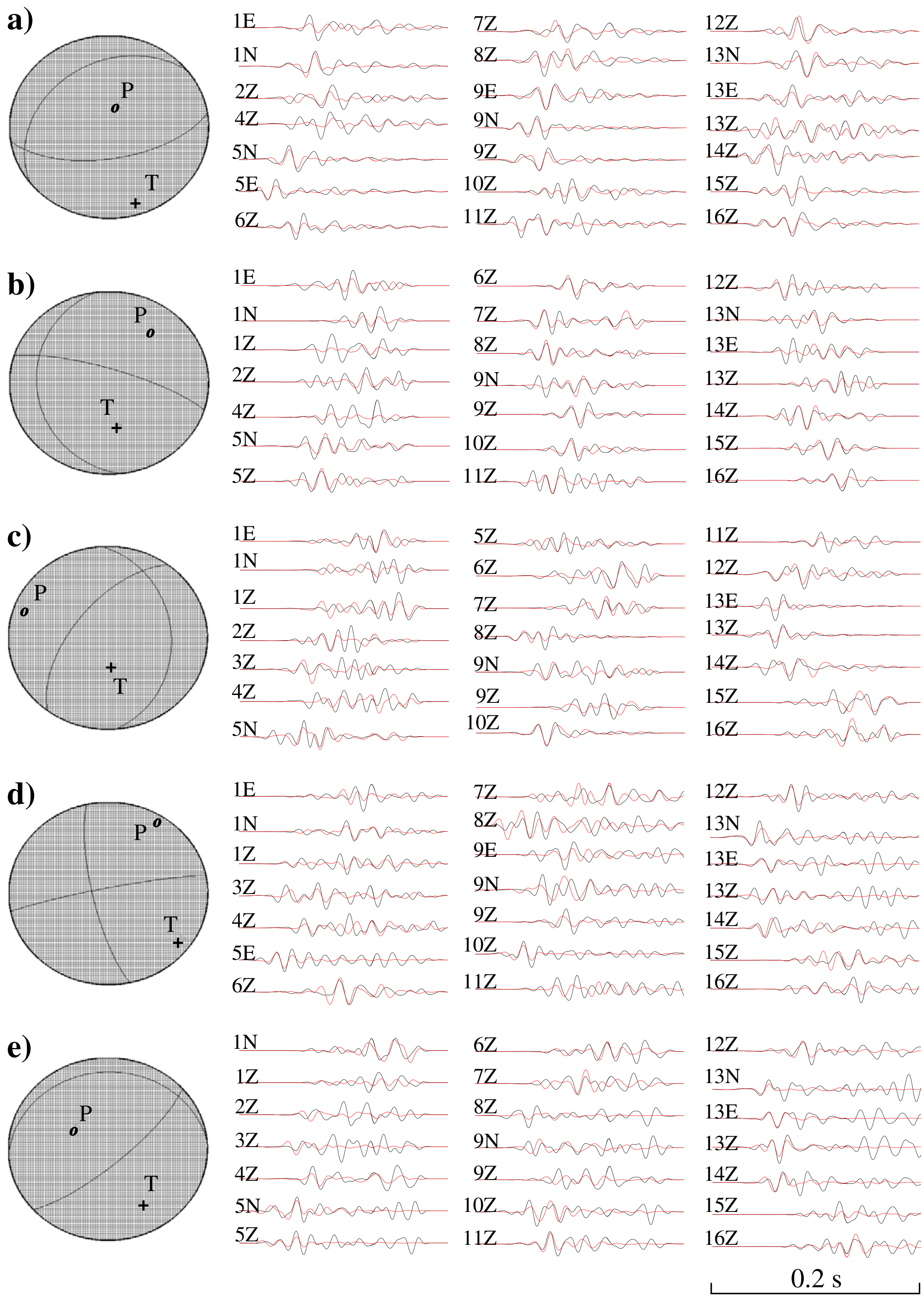

Fig. 12. Moment tensor inversion of blasts. Plots (a–e) show the focal mechanisms (left) and the fit between the synthetic waveforms and data (right) for blasts 1 to 5. Synthetic waveforms are plotted in red, observed data in black; geophone numbers and components are indicated for each trace.

as the fits between data and synthetic waveforms. Table 4 presents the strike, rake and dip of the DC components as well as percentages of the DC and non-DC components including their errors.

The basic difference between the results for blasts and events is the percentage of the isotropic component: it is high and positive for the blasts, but high and negative for the events. The maximum ISO percentage is obtained for blast 5 reaching almost 81%. In this case, the DC component is minor and unstable, the mean deviation of the P/T axes being 25°. This indicates that the DC component is mostly caused by numerical errors. For the other blasts, the DC percentage is higher and the mean deviation of the P/T axes smaller. Thus, it may reflect the presence of some other minor mechanisms such as shearing or opening of tensile cracks induced during blasting. The negative values of the ISO and CLVD components for the events indicate the presence of a significant non-shear focal mechanism probably caused by the collapse of rock due to excavation. The

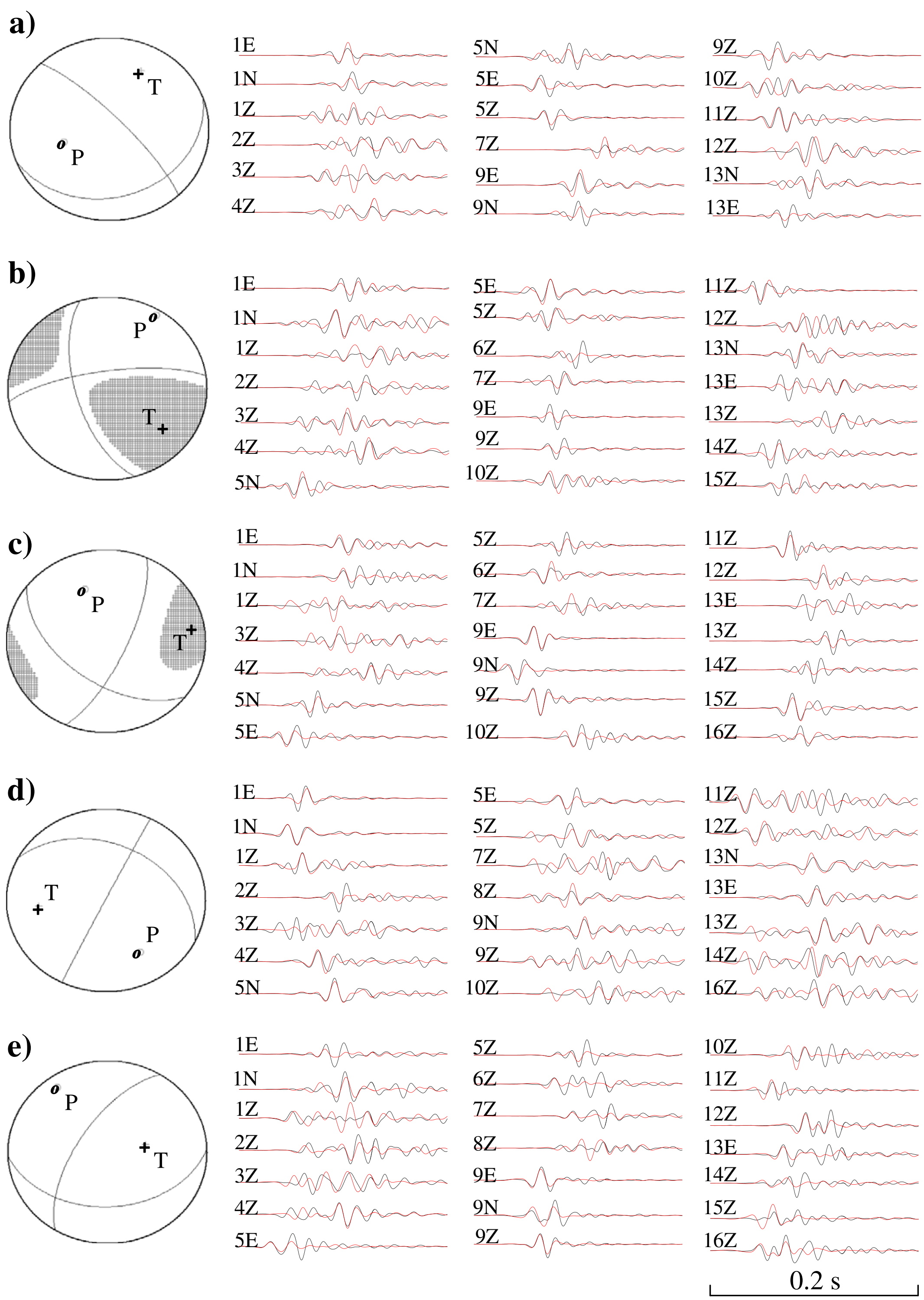

Fig. 13. Same as Fig. 12, but for the moment tensor inversion of events.

negative values of both ISO and CLVD components are consistent with the model of tensile earthquakes exhibiting compressive motions at the source (Vavryčuk, 2011).

The errors of the results significantly vary both among blasts and events. The best accuracy is obtained for blast 1 and event 5. Their moment tensors are stable even when higher values of noise are applied, e.g., 50% or 100%. This is probably due to very accurate source locations and, consequently, well reproduced Green's functions.

8. Conclusions

The structural model of mines is usually very complex, especially due to the strong contrasts in seismic velocities at tunnels and mined-out cavities. Rays can be strongly curved and small changes in source positions may lead to remarkable changes in ray paths. Consequently, the radiated wave field is sensitive to the source location and may be very complex containing pronounced and long coda waves. Therefore, the determination of source parameters and

Table 4
Focal mechanisms of blasts and events. Φ, δ, and λ are strike, dip and rake of the retrieved focal mechanism, δ(P/T) is the mean error in the orientation of the focal mechanism (for the definition, see the text), and δDC, δCLVD and δISO are the mean errors of the DC, CLVD and ISO, respectively.

	Φ [°]	δ [°]	λ [°]	DC [%]	CLVD [%]	ISO [%]	δ(P/T) [°]	δDC [%]	δCLVD [%]	δISO [%]
Blasts										
Blast 1	84.8	66.7	−71.8	19.5	14.6	65.9	2.8	3.3	4.0	2.8
Blast 2	173.0	28.2	152.9	38.5	3.1	58.4	4.7	7.3	4.9	4.1
Blast 3	217.2	60.9	113.1	21.2	−12.7	66.1	8.3	4.5	3.9	3.6
Blast 4	167.4	77.2	174.9	19.9	15.0	65.1	6.1	6.9	4.3	4.2
Blast 5	48.5	76.4	−100.0	12.1	−6.6	81.3	25.3	5.4	4.4	3.7
Events										
Event 1	69.5	27.0	−154.2	4.9	−36.2	−58.9	13.5	10.0	10.9	19.0
Event 2	261.9	74.2	27.3	63.7	−19.6	−16.7	10.7	13.0	12.6	9.2
Event 3	127.2	53.5	−158.5	52.6	−10.3	−37.1	3.0	8.7	4.7	6.6
Event 4	297.4	38.8	−178.8	10.6	−24.7	−64.7	7.5	7.3	5.1	3.9
Event 5	211.7	64.7	57.9	38.2	−0.6	−61.2	2.4	3.6	2.6	2.9

moment tensors from radiated waves in a complex mining environment is an extremely difficult task. Since the moment tensor inversion is sensitive to time shifts due to mislocation or to inaccuracies of the velocity model, the inversion requires highly accurate locations and well reproduced Green's functions of the complete wave field. In addition, earthquake mechanisms in mines mostly include non-double-couple components, which are difficult to retrieve even with simple velocity models.

We compute accurate locations using the eikonal solver by Podvin and Lecomte (1991). The solver is applicable even in very heterogeneous media, provided the detailed geometry of tunnels and cavities is well documented, and the velocities of rocks are known with good accuracy. Green's functions required for the waveform moment tensor inversion for such a complex mining environment should be computed by full waveform modelling capable of reproducing complex interactions of waves and structures. For this task, we used the 3-D finite difference visco-elastic code E3D (Larsen and Grieger, 1998) on a model with a spatial sampling of 2 m and a sampling frequency of 10 kHz. In order to reduce the computational time, the reciprocity principle is employed. Note that accurate Green's functions are essential for the success of the inversion and that their calculation is the most computationally demanding step of the whole inversion procedure.

Compared to the computation of Green's functions, the moment tensor inversion from waveforms is computationally straightforward. We used an inversion in time domain and solved for moment tensors using a generalized linear inversion. To suppress the sensitivity of the inversion to inaccuracies in source locations and velocity model, we filtered the data in the frequency range from 30 to 80 Hz. The analysis of 5 blasts and 5 induced microseismic events proves that the moment tensor inversion is successful. As expected, the blasts display a high percentage of positive isotropic components. However, we cannot exclude that minor shear faulting was triggered during the blasting. On the other hand, the microseismic events display significant negative ISO and CLVD components. This indicates that the predominant source mechanism of the events is probably related to collapse of rock due to excavation activity.

Supplementary data to this article can be found online at http://dx.doi.org/10.1016/j.tecto.2012.12.035.

Acknowledgements

We thank Katja Salaha (INMET Mining Co.) and ISS International Ltd. (transformed to IMS Ltd. in 2010) for access to the mine model and to the in-mine data. We thank S. Larsen for his E3D code and H. N. Gharti for the computation of travel times using the eikonal solver as well as his help with the application of E3D. Additionally, we thank the editor Hans Thybo and two anonymous reviewers who greatly helped to enhance the comprehensibility and accurateness of our manuscript. The work was funded by the ACUPS Project (financed by the Norwegian Research Council and industry partners BP, Statoil and Total; Grant No. 176016), by the SafeCO2 Project (financed by the Norwegian Research Council and industry partners ConocoPhillips, Lundin, Octio, READ and Statoil; Grant No. 189994), by the Grant Agency of the Academy of Sciences of the Czech Republic, Grant No. IAA300120801, by the Grant Agency of the Czech Republic, Grant No. P210/12/1491, and by the European Community's FP7 Consortium Project AIM "Advanced Industrial Microseismic Monitoring", Grant Agreement No. 230669. The figures were produced using the open-source visualisation software packages ParaView and GMT (Wessel and Smith, 1991).

References

Aki, K., Richards, P.G., 2002. Quantitative Seismology. University Science books, Sausalito, California.
Červený, V., Soares, J.E.P., 1992. Fresnel volume ray tracing. Geophysics 57 (7), 902–915.
Dahm, T., Manthei, G., Eisenblätter, J., 1998. Relative moment tensors of thermally induced microcracks in salt rock. Tectonophysics 289, 61–74.
Dahm, T., Manthei, G., Eisenblätter, J., 1999. Automated moment tensor inversion to estimate source mechanisms of hydraulically induced micro-seismicity in salt rock. Tectonophysics 306, 1–7.
Domański, B., Gibowicz, S.J., Wiejacz, P., 2002. Source time function of seismic events at Rudna copper mine, Poland. Pure and Applied Geophysics 159, 131–144.
Gharti, H.N., Oye, V., Roth, M., 2008. Travel times and waveforms of microseismic data in heterogeneous media. 78th Ann. Int. Meeting SEG, Exp. Abstr, 27, pp. 1337–1341.
Gharti, H.N., Oye, V., Roth, M., Kühn, D., 2010. Automated microearthquake location using envelope stacking and robust global optimization. Geophysics 75 (4), MA27–MA46. http://dx.doi.org/10.1190/1.3432784.
Hagedoorn, J.G., 1954. A process of seismic reflection interpretation. Geophysical Prospecting 2 (2), 85–127. http://dx.doi.org/10.1111/j.1365-2478.1954.tb01281.x.
Husen, S., Kissling, E., 2001. Local earthquake tomography between rays and waves: fat ray tomography. Physics of the Earth and Planetary Interiors 123, 127–147.
Jost, M.L., Büsselberg, T., Jost, O., Harjes, H.P., 1998. Source parameters of the injection-induced microearthquakes at 9 km depth at the KTB deep drilling site, Germany. Bulletin of the Seismological Society of America 88, 815–832.
Julian, B.R., Miller, A.D., Foulger, G.R., 1998. Non-double-couple earthquakes 1: theory. Reviews of Geophysics 36, 525–549.
Larsen, S., Grieger, J., 1998. Elastic modelling initiative: part 3—3-D computational modelling. 68th Ann. Int. Meeting SEG, Exp. Abstr, pp. 1803–1806.
Ledger, A., 1999. Stress measurement in the 1125 m level. Outokumpu Mining Pyhäsalmi Mine Oy. Report for Rock Mechanics Technology Ltd, Pyhäsalmi Mine Oy (7 pp.).
Luo, X., Yu, K., Hatherly, P., Zhang, X., 2001. Microseismic monitoring of rock fracturing under aquifers in longwall coal mining. 71th Ann. Int. Meeting SEG, Exp. Abstr, pp. 1521–1524.
Manthei, G., 2005. Characterization of acoustic emission sources in a rock salt specimen under triaxial compression. Bulletin of the Seismological Society of America 95 (5), 1674–1700.
McNally, K.C., McEvilly, T.V., 1977. Velocity contrast across the San Andreas Fault in Central California: small-scale variations from P-wave nodal plane distortion. Bulletin of the Seismological Society of America 67 (6), 1565–1576.
Menke, W., 1989. Geophysical Data Analysis: Discrete Inverse Theory. Int. Geophys. Series 45, Academic Press, New York.
Miller, A.D., Foulger, G.R., Julian, B.R., 1998. Non-double-couple earthquakes. 2. Observations Reviews of Geophysics 36 (4), 551–568. http://dx.doi.org/10.1029/98RG00717.
Oye, V., Roth, M., 2003. Automated seismic event location for hydrocarbon reservoirs. Computers and Geosciences 29, 851–863.
Oye, V., Bungum, H., Roth, M., 2005. Source parameters and scaling relations for mining-related seismicity within the Pyhäsalmi ore mine, Finland. Bulletin of the Seismological Society of America 95 (3), 1011–1026. http://dx.doi.org/10.1785/0120040170.
Phillips, W.S., Fairbanks, T.D., Rutledge, J.T., Anderson, D.W., 1998. Induced microearthquake patterns and oil-producing fracture systems in the Austin chalk. Tectonophysics 289, 153–169.
Phillips, W.S., Rutledge, J.T., House, L.S., Fehler, M.C., 2002. Induced microearthquake patterns in hydrocarbon and geothermal reservoirs: six case studies. Pure and Applied Geophysics 159, 345–369.
Podvin, P., Lecomte, I., 1991. Finite difference computation of traveltimes in very contrasted velocity models: a massively parallel approach and its associated tools. Geophysical Journal International 105, 271–284.
Puustjärvi, H., 1999. Pyhäsalmi Modeling Project, Section B. Geology. Technical Report, Geological Survey of Finland and Outokumpu Mining Oy (66 pp.).
Reinecker, J., Heidbach, O., Tingay, M., Connolly, P., Müller, B., 2004. The 2004 release of the World Stress Map. Available online at www.world-stress-map.org.
Rudajev, V., Sileny, J., 1985. Seismic events with non-shear components, II, Rockbursts with implosive source component. Pure and Applied Geophysics 123, 17–25.
Rutledge, J.T., Phillips, W.S., Schuessler, B.K., 1998. Reservoir characterization using oil-production-induced microseismicity, Clinton County, Kentucky. Tectonophysics 289, 129–152.

Šílený, J., 2009a. Resolution of non-double-couple mechanisms: simulation of hypocenter mislocation and velocity structure mismodeling. Bulletin of the Seismological Society of America 99, 2265–2272.

Šílený, J., 2009b. Moment tensors of mining tremors—detection tool of the mode of rock-mass fracturing: mechanism of deep events on October 24 and October 12, 2005 in Moab Khotsong mine, S. Africa. In: Tang, C. (Ed.), Controlling seismic hazard and sustainable development of deep mines. : Proc. of the 7th Int. Symp. on Rockburst and Seismicity in Mines. Rinton Press Inc., USA, pp. 399–406.

Šílený, J., Milev, A., 2008. Source mechanism of mining induced seismic events—resolution of double couple and non double couple models. Tectonophysics 456, 3–15.

Sokos, E., Zahradník, J., 2008. ISOLA—a Fortran code and Matlab GUI to perform multiple point source inversion of seismic data. Computers and Geosciences 34, 967–977.

Spottiswoode, S.M., Milev, A.M., 1998. The use of waveform similarity to define planes of mining-induced seismic events. Tectonophysics 289, 51–60.

Trifu, C.-I., Angus, D., Shumila, V., 2000. A fast evaluation of the seismic moment tensor for induced seismicity. Bulletin of the Seismological Society of America 90, 1521–1527.

Urbancic, T.I., Rutledge, J.T., 2000. Using microseismicity to map Cotton Valley hydraulic fractures. 70th Ann. Int. Meeting SEG, Exp. Abstr, pp. 1444–1448.

Vavryčuk, V., 2007. On the retrieval of moment tensors from borehole data. Geophysical Prospecting 55, 381–391. http://dx.doi.org/10.1111/j.1365-2478.2007.00624.x.

Vavryčuk, V., 2011. Tensile earthquakes: theory, modeling and inversion. Journal of Geophysical Research 116, B12320. http://dx.doi.org/10.1029/2011JB008770.

Vavryčuk, V., Kühn, D., 2012. Moment tensor inversion of waveforms: a two-step time-frequency approach. Geophysical Journal International 190 (3), 1761–1776. http://dx.doi.org/10.1111/j.1365-246X.2012.05592.x.

Vavryčuk, V., Bohnhoff, M., Jechumtálová, Z., Kolář, P., Šílený, J., 2008. Non-double-couple mechanisms of micro-earthquakes induced during the 2000 injection experiment at the KTB site, Germany: a result of tensile faulting or anisotropy of a rock? Tectonophysics 456, 74–93. http://dx.doi.org/10.1016/j.tecto.2007.08.019.

Vinje, V., Iversen, E., Åstebøl, K., Gjøystdal, H., 1996a. Estimation of multivalued arrivals in 3D models using wavefront construction—part I. Geophysical Prospecting 44 (5), 819–842.

Vinje, V., Iversen, E., Åstebøl, K., Gjøystdal, H., 1996b. Part II: tracing and interpolation. Geophysical Prospecting 44 (5), 843–858.

Wallace, T., Given, J., Kanamori, H., 1982. A discrepancy between long- and short-period mechanisms of earthquakes near the Long Valley caldera. Geophysical Research Letters 9 (10), 1131–1134.

Wessel, P., Smith, W.H.F., 1991. Free software helps map and display data. EOS. Transactions of the American Geophysical 72, 441.

Wong, I.G., McGarr, A., 1990. Implosional failure in mining induced seismicity: a critical review. In: Fairhurst, C. (Ed.), Rockbursts and Seismicity in Mines, Balkema, pp. 45–51.

Wong, I.G., Humphrey, J.R., Adams, J.A., Silva, W.J., 1989. Observations of mine seismicity in the eastern Wasatch Plateau, Utah, USA. A possible case of implosional failure. Pure and Applied Geophysics 129, 369–405.